

Observation and analysis of speciated atmospheric mercury in Shangri-la, Tibetan Plateau, China

H. Zhang^{1,2}, X. W. Fu¹, C.-J. Lin^{1,3,4}, X. Wang^{1,2}, X. B. Feng^{1*}

¹ State Key Laboratory of Environmental Geochemistry, Institute of Geochemistry, Chinese Academy of Sciences, Guiyang 550002, PR China (E-mail: fengxinbin@vip.skleg.cn)

² University of Chinese Academy of Sciences, Beijing 100049, PR China

³ Department of Civil Engineering, Lamar University, Beaumont, Texas 77710, United States

⁴ College of Energy and Environment, South China University of Technology, Guangzhou 510006, China

*: Corresponding author

Abstract

This study reports the concentrations and potential sources of **speciated** atmospheric mercury at the Shangri-La Atmosphere Watch Regional Station (SAWRS), a pristine high-altitude site (3580 m above sea level) in Tibetan Plateau, China. Total gaseous mercury (TGM, defined as the sum of Gaseous Elemental Mercury, GEM, and Gaseous Oxidized Mercury, GOM), GOM and particulate-bound mercury (PBM) were monitored from November 2009 to November 2010 to investigate the characteristics and potential influence of the Indian summer monsoon (ISM) and the **Westerlies** on the atmospheric transport of mercury. The mean concentrations (\pm standard deviation) of TGM, PBM and GOM were 2.55 ± 0.73 ng m⁻³, **38.82 ± 31.26 pg m⁻³** and **8.22 ± 7.90 pg m⁻³**, respectively. A notable seasonal pattern of TGM concentrations was observed with higher concentrations at the beginning and the end of the ISM season. **High TGM concentrations (> 2.5 ng m⁻³) were associated with the transport of dry air that carried regional anthropogenic emissions from both Chinese domestic and foreign (e.g., Burma, Bengal Bay, and north India) sources based on analysis of HYSPLIT4 backward trajectories. Somewhat lower PBM and GOM levels during the ISM period were also observed and attributed to the enhanced wet scavenging. The high GOM and PBM is likely be caused by local photochemical transformation under low RH and the domestic biofuel burning in cold seasons.**

Keywords: Atmospheric mercury, Shangri-La, Long-range transport, Indian summer monsoon.

1 Introduction

Mercury (Hg) is a persistent toxic pollutant released to the atmosphere from both anthropogenic and natural sources (Pirrone et al., 1996; Pirrone et al., 2001; Carpi and Lindberg, 1998). Due to its volatility, GEM can be transported over a long distance. Hg interconverts among GEM, GOM and PBM and enters terrestrial and aquatic ecosystems in remote areas via dry and wet deposition (Johansson et al., 2001). Deposited Hg can be converted into methyl-mercury, a potent neurotoxin that bioaccumulates and biomagnifies in the food chain and causes severe public health concerns (Lindqvist, 1991; Sunderland et al., 2009). In the atmosphere, GEM is the predominant species and accounts for >90% of total Hg (Iverfeldt and Lindqvist, 1986; Schroeder and Munthe, 1998). The global background of GEM is 1.5-1.7 ng m⁻³ and 1.1-1.3 ng m⁻³ in the Northern and Southern Hemisphere. Typical concentrations of GEM, GOM and PBM measured at remote sites are in the ranges of 1–4 ng m⁻³, 3–70 pg m⁻³ and 7–100 pg m⁻³, respectively (Valente et al., 2007; Pfaffhuber et al., 2012). In the Arctic, the GEM, PBM and GOM median concentrations are 1.6 ng m⁻³, 11.3 and 3.2 pg m⁻³, respectively (Steffen et al., 2014). In Antarctica, the mean annual GEM concentration of 0.93±0.19 ng m⁻³ is in good agreement with recent southern-hemispheric measurements (Pfaffhuber et al., 2012).

Observations of atmospheric Hg are important to understand its global biogeochemical cycling. Long-term and continuous measurements at remote sites are particularly valuable because such datasets help in understanding the seasonal trends and transport patterns of atmospheric Hg in a given region (Li and Lee, 2014; Pirrone et al., 2010b; Driscoll et al., 2013). In addition, the observations provide data for constraining atmospheric models of Hg. To address the data need, there have been ongoing efforts to establish monitoring networks, including the atmospheric mercury network (AMNet) in North America and the global mercury observation system (GMOS) (Sprovieri et al., 2013; Gay et al., 2013). Monitoring of speciated atmospheric Hg at remote sites is challenging due to issues related to instrumental maintenance, accessibility to the sites and other logistic limitations. To date, the availability of speciated atmospheric Hg observations is inadequate for a thorough understanding of Hg chemical transport in different regions.

Shangri-La is located remotely in the southeastern corner of the Tibetan Plateau that extends from 25° to 45°N and from 70° to 105°E. This Plateau covers approximately one-quarter of the land area in Mainland China with a mean elevation of more than 4,000 m above sea level. Given the location between South and East Asia, the levels of air pollutants at Shangri-La are potentially influenced by the two largest source regions in the world. There are an increasing number of studies highlighting the large and increasing Hg

emissions in fast developing countries (Pirrone et al., 2010). China is the largest Hg emitter in the world, despite its continued effort in Hg emission reduction (Streets et al., 2005; Pacyna et al., 2006). India, with the world's fourth biggest coal reserve, is another rapidly growing economy whose Hg use and emission have been increasing over the last few decades (Sharma, 2003). Therefore, it is environmentally significant to better understand the trans-boundary transport of air pollutant emissions between China and India. Recent assessments suggested that the emissions in India are of global importance, especially to the Tibetan plateau where the long-range transport of black soot accelerates glacier melting (Xu et al., 2009). In addition, it has been suggested that Hg emissions from South Asia can be transported to the Tibetan plateau and deposit on glaciers through the Indian summer monsoon (ISM), which and has led to higher Hg concentrations in snow packs (Loewen et al., 2007; Zhang et al., 2012). Hg emissions from the biomass burning in Southeast Asia also represent a significant yet uncertain regional source (Pirrone et al., 2010b). In light of these perspectives, Shangri-La appears to be a strategic observational site for studying the long-range transport of Hg emitted from these sources.

In this study, we report the characteristics of the speciated atmospheric Hg at the SAWRS and analyze the potential source regions that contributed to the observed concentrations. In particular, we assess the role of the ISM and the Westerlies in the long-range transport of Hg. This study addresses of the GMOS objectives in establishing a global mercury monitoring network for ambient concentrations and deposition of Hg through ground-based observational platforms as well as oceanographic aircraft campaigns. The data within the GMOS network can be used for model assessment, for understanding the global biogeochemical cycling of Hg, and for establishing a global source-receptor relationship of Hg emissions. The program involves 24 partners around the world (GMOS, <http://www.gmos.eu/>).

2 Materials and methods

2.1 Measurement site description

Fig. 1 shows the locations of SAWRS and large Asian cities. The SAWRS (28°01'N, 99°44'E, 3580 m above sea level) is a remote highland site located in the Hengduan Mountains area southeast of the Tibetan Plateau. The SAWRS is near a mountaintop and surrounded by alpine forest and 30 km north of Shangri-La city. The largest point sources near SAWRS are coal fire power plants in Kunming city, capital of Yunnan province, which is ~500 km to the southeast. Other large cities (Chengdu, Guiyang and Chongqing) are east of Shangri-La (~1000 km). India and Bengal are located to the west of SAWRS and Southeast Asia (in this study, it is defined as the region 92°E-140°E, 10°S-23°26'N). It has a cold and dry

winter that lasts 5 months from late October to April before onset of ISM. Its annual average temperature is 5.1 °C. The average temperature is -1.4 °C from December to February and 12.4 °C from June to August (Table 1). The population density in Shangri-La is approximately 10 persons per square kilometer. As the SAWRS is surrounded by the forest, there are no large-scale industrial activities and fossil fuel consumption in the area. Domestic biofuel burning for cooking and house heating is the main emission source, which release $<10 \text{ g km}^{-2}\text{y}^{-1}$ of Hg annually (AMAP/UNEP, 2013).

2.2 Sampling methods and analysis

2.2.1 Measurements of atmospheric TGM, PBM and GOM

TGM was monitored between November 2009 and November 2010. The inlet of the heated Teflon sampling tubing for TGM monitoring was set up at 10 m above ground. Measurement of the TGM concentrations was performed using an automated Hg vapor analyzer Tekran Model 2537A (Tekran Instruments Corp., Toronto, Ontario, Canada). The instrument allows continuous measurement of TGM (GEM+GOM) in ambient air through a cycle of gold trap amalgamation, thermal desorption and detection by cold vapor atomic fluorescence spectrometry ($\lambda=253.7 \text{ nm}$). The precision, accuracy, stability of the instrument have been documented extensively (Gay et al., 2013b). Tekran 2537A automatically calibrates for GEM every 25 h using an internal permeation source, which provides approximately 1 pg s^{-1} of GEM at 50 °C into a zero air stream. External calibration using a Tekran 2505 with manual injections of known concentrations of GEM was performed every 4 months, and the accuracy of the analyzer based on manual injection calibrations was 96.84%. The precision is $<2\%$ with a detection limit $<0.1 \text{ ng m}^{-3}$. PBM in ambient air was removed using a 47mm diameter Teflon filter (pore size $0.2 \mu\text{m}$). For sampling at the reduced ambient pressure at the site, a lower sampling rate of 0.75 l min^{-1} (at standard temperature and pressure, as compared to the typical 1 l min^{-1}) at sampling interval of 5 minutes was used during the entire campaign (Fu et al., 2012a).

A denuder-based sampling unit (separate from the TGM sampling train) was used for sampling PBM and GOM. Detailed schematics of the sampling unit, instrumental configuration and field illustrations are shown in the supplementary information (Fig. S1-S5). In short, the annular denuder tubes (URG Corporation) are made of quartz with the inner wall coated with KCl for GOM sampling. An integrated elutriator/acceleration jet and a glass impactor plate capable of removing coarse particles ($>2.5 \mu\text{m}$) were installed before the inlet of the denuder. The PBM and GOM samples were collected continuously and analyzed immediately. A fresh glass impactor was replaced upon completing each sampling cycle. PBM (defined as Hg associated with particles $<2.5 \mu\text{m}$) was collected on 47 mm diameter quartz filters housed in a Teflon filter holder downstream of the denuder. The quartz filters for sampling PBM were the

Whatman Grade QM-H Quartz Filter from GE healthcare (<http://www.gelifesciences.com/webapp/wcs/stores/servlet/catalog/zh/GELifeSciences/>). This is a pure quartz fiber filter with low heavy metal content, and can be used at temperatures up to 900 °C. Each quartz filter was used for one sampling and analysis cycle to prevent potential deformation and contamination. A KCl-coated denuder was installed in the sampling unit with an impactor. Once a sampling period was completed, the prepared PBM and GOM sampling unit were installed swiftly for the next sampling cycle. The typical replacement time of each denuder and filter was very short (almost 10 minutes) (Xiao et al., 1997; Landis et al., 2002a; Feng et al., 2000). Both the PBM filter and denuder were positioned vertically. The inlets were located at 1.5 m above ground. An electronic temperature-controlled heating tape was utilized to maintain the temperature of the denuder sampling train at 40–50 °C above the ambient temperature to prevent water condensation on the KCl coating and the wall loss of GOM in the sampling tube (Feng et al., 2000). The sampling flow rate (10 L min⁻¹) for both GOM and PBM was controlled by mass-flow controllers (MKS, USA) calibrated to standard atmospheric pressure (0 °C and 1013 mbar). Two identical units were deployed: one was used for the air sampling while the other was undergoing Hg desorption and detection. The GOM and PBM were sampled simultaneously and each analysis cycle was two hours. Using this sampling protocol, twelve GOM and twelve PBM samples were collected per day. The denuder and filter were analyzed immediately after air sampling.

Analytical procedures for GOM described by Munthe et al. (2001), Lynam et al. (2002) and Landis et al. (2002a) were followed. The PBM analysis was achieved using a heating method. After sampling, Hg contents were determined via pyrolysis followed by Tekran 2537A detection. First, the Tekran 2537A pulled Hg-free air (0.5 L min⁻¹) through the filter trap and denuders for two sample cycles (10 min) to confirm the zero background for ensuring no leaks in the system. The filter was placed into the trap using an installation tool (Nichrome wire with a hook at one end). Then, the trap and denuders were rapidly heated to 900 and 500 °C using a Lindberg Blue clamshell furnace for three heating cycles (15 min) to convert PBM and GOM into GEM, which is analyzed by the Tekran 2537A. To prevent the end caps of denuder and trap from emitting mercury during heating, air cooling was applied on both ends of the denuder. Typically, a signal of <2 pg was typically observed in the third heating cycle, which is indistinguishable from the system blank. The PBM traps and denuders were then cooled by a cooling fan in the third step (Fig. S4-S6).

Four sampling campaigns were carried out for PBM and GOM measurements: January 17- February 1, May 8-18, July 10-25, and October 28 to November 11, 2010. The selected periods represented four seasonal observations. Before sampling, the denuders were cleaned by pyrolysis to obtain the blank

(1.67 ± 0.66 pg, $N=12$). The quartz filter was cleaned by heating at 850°C for 30 min. A somewhat higher blank (6.62 ± 2.69 pg, $N=20$) was observed. The denuder and quartz filter blanks were used for correcting the GOM and PBM concentrations by subtracting the mean blank from the detected concentration. This GMOS standard operational procedure was followed to ensure data quality. For quality assurance, the A/B cartridge bias of Tekran 2537A must be $< 10\%$. Using data quality assurance criteria of GMOS, the data completeness in this study was 92.6% of the total sample size.

2.2 Meteorological data and backward trajectory calculation

Meteorological parameters including hourly wind direction (WD), wind speed (WS), air temperature (AT), relative humidity (RH) and rainfall (RF) were continuously monitored via an automatic weather station (PH-SLFH, made in China) at the SAWRS. The Indian monsoon indices (IMI), defined as the difference of 850 hPa zonal winds between a southern region of 5°N – 15°N , 40°E – 80°E and a northern region of 20°N – 30°N , 70°E – 90°E (Wang and Fan, 1999; Wang et al., 2001), were obtained online at the Asia-Pacific Air Data-Research Center (<http://apdrc.soest.hawaii.edu/projects/monsoon/realtime-monidx.html>). The IMI reflects both the intensity of the tropical westerly monsoon and the lower-tropospheric vorticity anomalies associated with the ISM trough. With a positive IMI, the study region was expected to be influenced by air transport caused by the ISM, characterized by wet air flow from the Indian Ocean and high rainfall in southern and southeastern Asia. A zero IMI indicates weak air movement. A negative IMI indicates that northerly winds push the air mass back the Indian Ocean. Five-day backward trajectories were calculated using HYSPLIT4 (Wang et al., 2009) to assess the transport pathways (<http://www.arl.noaa.gov/ready/hysplit4.html>). The Global Data Assimilation System (GDAS) meteorology archived by the Air Resource Laboratory of National Oceanic and Atmospheric Administration (NOAA) were used as the input (<ftp://arlftp.arlhq.noaa.gov/pub/archives/gdas1/>). The spatial and temporal resolution of the met data is $1^\circ \times 1^\circ$ and 6-hour, respectively. The arrival height of the trajectories is 500 m above ground. The back trajectory endpoints were recorded at 6-h intervals (02:00, 08:00, 14:00, 20:00 LT).

Cluster analysis of the back trajectories was performed to obtain the synoptic transport pattern to the site. Clustering started by assigning each trajectory to its own cluster, so that there was the same number of clusters as the number of trajectories (i.e., one trajectory in each cluster). For each iteration step, the cluster number was reduced by one as two clusters were merged together. For every combination of trajectory pairs, the cluster spatial variance (SV), defined as the sum of the squared distances between the endpoints of the cluster's component trajectories and the mean of the trajectories in that cluster, was computed. Then the total spatial variance (TSV), defined as the sum of all cluster SV and increased for

each additional inclusion of a trajectory, was calculated. The clustering process continued until the TSV suddenly increased by a large value, indicating that the included trajectory in the given iteration was not similar to the included trajectories included in a cluster. Such processes continued until the iterative step just before the large increase in the change of TSV gave the final number of clusters. Once the number of clusters was determined, the endpoints of trajectories in the same cluster were averaged and shown in the map (Wang et al., 2009; Dorling et al., 1992). Similar analysis has been used in previous studies (Rozwadowska et al., 2010; Landis et al., 2002b; Fu et al., 2012a).

Potential Source Contribution Function (PSCF) was performed to analyze and estimate the influence of the potential sources. The PSCF value for the ij_{th} cell is then defined as:

$$PSCF_{ij} = \frac{M_{ij}}{N_{ij}} \times W_{ij} \quad (1)$$

Where M_{ij} represents the number of trajectory endpoints associated with 85 or higher percentiles of the observed TGM, N_{ij} is the number of endpoints associated with 50 or higher percentiles of the observed TGM. To reduce the effect of small values of N_{ij} , the PSCF values were multiplied by a weight function W_{ij} to reflect the uncertainty in the values for these cells (Polissar et al., 2001). The endpoints reaching the ground were excluded in the PSCF calculation. Overall, more than 27,000 endpoints were included for the calculation. The weighting function was defined as:

$$W_{ij} = \begin{cases} 1.0 & N_{ij} > 3Avg \\ 0.7 & 1.5Avg < N_{ij} \leq 3Avg \\ 0.4 & Avg < N_{ij} \leq 1.5Avg \\ 0.2 & N_{ij} \leq Avg \end{cases} \quad (2)$$

where Avg is the average endpoints in each grid cells.

3 Results and discussion

3.1. Distribution and influences of potential regional sources.

The 5-min time series plot of the TGM concentrations is shown in Fig. 2. It ranged from 1.03 to 13.59 ng m⁻³ with a mean of 2.55±0.73 ng m⁻³ (Table 1). Spikes of high TGM concentrations were observed from late April through early May (5.87 ng m⁻³), from late June through early July (4.58 ng m⁻³), and in late September (4.74 ng m⁻³). The three high TGM events occurred during the months when the ISM was prevailing, suggesting the ISM played an important role in the high TGM observed at the SAWRS (further discussed in Section 3.3). The levels of TGM at the SAWRS were much lower than those observed in southwestern Chinese cities [9.7±10.2 ng m⁻³ in Guiyang (Fu et al., 2011); 6.74±0.37 ng m⁻³ in Chongqing, (Yang et al., 2009)]. It was also lower than the background concentrations observed at Mt. Leigong in Guizhou province [2.80 ± 1.51 ng m⁻³, (Fu et al., 2010) and Mt. Gongga in Sichuan province

($3.98 \pm 1.62 \text{ ng m}^{-3}$, (Fu et al., 2008)], but higher than those observed at Mt. Changbai ($1.60 \pm 0.51 \text{ ng m}^{-3}$) in Northeast China and at Mt. Waliguan (WLG) Baseline Observatory ($1.98 \pm 0.98 \text{ ng m}^{-3}$) in Tibetan Plateau (Fu et al., 2012a; Fu et al., 2012b). The TGM mean concentration at the SAWRS was higher than the global background ($1.5\text{--}1.7 \text{ ng m}^{-3}$) in the Northern Hemisphere and $1.1\text{--}1.3 \text{ ng m}^{-3}$ in the Southern Hemisphere (Lindberg et al., 2007). As a remote background site, the TGM level was mainly influenced by the long-range transport and possibly weak local sources (Obrist et al., 2008; Fu et al., 2012a). The SAWRS is located between East Asia and South Asia where large Hg emission sources exist (Fig. 1). The TGM concentrations measured at Korean and Japanese background sites were also much higher due to the nearby emission sources and the prevailing westerly wind [4.61 ng m^{-3} at Global Atmospheric Watch Station in An-Myun Island of Korea, (Nguyen et al., 2007); 2.04 ng m^{-3} at Cape Hedo Station in Okinawa Island of Japan, (Jaffe et al., 2005)]. The GEM level of Lulin Atmospheric Background Station in Taiwan (1.73 ng m^{-3}) was comparatively lower. The mean TGM concentration at SAWRS was higher than the background sites in North America and Europe [mean 1.5 ng m^{-3} from the North America Atmospheric Mercury Network, $1.4\text{--}1.8 \text{ ng m}^{-3}$ at Mace Head and Zingst of Europe, (Kock et al., 2005; Gay et al., 2013b)]. The elevated background level of TGM at the SAWRS is likely due to strong regional sources in Asia.

The measured TGM concentration exhibited a strong dependence on wind direction. Higher TGM levels ($2.5\text{--}2.7 \text{ ng m}^{-3}$) were frequently associated with northerly winds that carried domestic emissions from West China to the site (Fig. 3). The elevated TGM concentrations ($2.5\text{--}2.6 \text{ ng m}^{-3}$) associated with the southerly winds could be caused by a combination of the regional emission sources in South Asia and Shangri-La County. The wind flows from the east and west contained lower TGM concentrations ($2.3\text{--}2.5 \text{ ng m}^{-3}$). The mountain ranges in Shangri-La area run in the north-south direction. The air masses in the east-west direction needed to cross high mountains to reach the SAWRS. When the air flow climb up to Shangri-La, the cumulus process (i.e., the vertical mixing that causes the dilution of an air mass and the condensation of water vapor at higher altitude) could lead to dilution of the air masses and scavenging of divalent mercury into atmospheric water, resulting in lower TGM concentrations. Fig. 4 displays the average diurnal trend of WD and WS along with those of TGM, GOM and PBM. The WD was predominantly southerly and changed from southeast (daytime) to southwest (nighttime). WS and TGM were slightly higher during daytime. Since the SAWRS is located on a small mountaintop in Hengduan Mountain area, the terrain could affect local air circulation. It is possible that diurnal mountain valley breezes played a significant role in the vertical mixing. During daytime, air near the valley heats up faster than the air at the high altitude. The air mass rapidly rose and brought the Hg trapped in the boundary layer to the monitoring site. At nighttime, the cool air from the high mountains sank and carried the clean

1 air from higher altitude to the site (Fu et al., 2010).

2
3 The diurnal pattern of GOM at the SAWRS showed higher concentrations in the afternoon. The relative
4 humidity in the afternoon (14:00~20:00) was 58.24%, much lower than the 81.47% at night and in the
5 morning (21:00-13:00). The mean GOM concentration in the afternoon was 9.22 pg m^{-3} and 7.34 pg m^{-3}
6 for the other period. A possible reason is the lower relative humidity during the afternoon hours decreases
7 the scavenging of GOM into atmospheric water. Another explanation is the oxidation of Hg^0 caused by
8 the stronger solar radiation (Lindberg et al., 2002; Goodsite et al., 2004; Fain et al., 2009). The measured
9 PBM did not show a distinct diurnal trend. The observed diurnal pattern of TGM and GOM reflected the
10 influence of local meteorology and photochemical production.

11 12 13 **3.2 Seasonal patterns of TGM, GOM and PBM**

14 The seasonal statistics of the measured TGM, GOM, PBM, WS, AT, RH and RF are shown in Table 1.
15 The mean TGM concentration in winter was lowest (2.28 ng m^{-3}) in the four seasons. In addition,
16 temperature, RH and RF were lower in winter after the retreat of the ISM. During the period, dry air
17 masses, typically associated with high WS, from Tibetan plateau caused the lower observed TGM. The
18 TGM level was highest in spring (2.76 ng m^{-3}) and peaked in late April (Fig. 2) when RF, AT and RH
19 increased with the onset of the ISM. Statistical analysis indicates that the TGM concentrations in spring
20 were statistically higher than the levels in autumn ($P < 0.001$) and winter ($P = 0.004$) (Table S1). The high
21 TGM events were caused by the regional transport from the heavily industrial regions in Northwest China
22 (more details in Section 3.3), with a peak observed concentration of 13.59 ng m^{-3} . Elevated TGM
23 concentrations (mean= 2.71 ng m^{-3}) were also observed in autumn (Fig. 2), which was associated with
24 lower AT, RH and RF. During the ISM period, the mean TGM level was 2.51 ng m^{-3} , which was
25 accompanied by the higher RH and RF.

26
27 The variation of the monthly means of TGM, WS, AT and RH is shown in Fig.5. During the ISM season
28 (May to September), a negative correlation between mean TGM concentration and the RH was evident
29 ($r = -0.83$, $p < 0.001$). The likely reason is that during the ISM period, clean air masses and water vapor
30 from Indian Ocean can move inland and lead to high RH and low TGM. In addition, the cumulus process
31 also could cause dilution of Hg in the atmosphere during precipitation events. High RH can decrease the
32 Hg emission from the surface and enhance wet deposition of Hg, which could contribute a relatively
33 lower TGM level (Seo et al., 2012; Poissant and Casimir, 1998). The TGM concentrations in late autumn
34 and winter months were relatively lower than other months (except August), likely due to the high WS

and dry air masses from Tibetan plateau caused by the strengthening of Westerlies. The variability of WS in autumn and winter cannot explain the observed seasonal variation of TGM level in the two seasons.

Both GOM (Fig. 6a) and PBM (Fig. 6b) exhibited substantial seasonal variability. GOM concentrations in winter were significantly higher than the levels in other seasons ($P < 0.001$) (Table S2). The GOM concentrations were higher in autumn (mean: 7.60 pg m^{-3}) and peaked in winter (14.62 pg m^{-3}), about four times of the mean level in spring (3.20 pg m^{-3}). A similar pattern was observed at Storm Peak Laboratory (3220 m a.s.l.) in the Rocky Mountains of USA (Fain et al., 2009). In the cold season, the air mass arriving in Shangri-La was primarily carried by the Westerlies with relatively higher wind speed (mean = 2.34 m s^{-1} in winter). These air masses occasionally passed through strong source regions in South and Southeast Asia as well as local anthropogenic sources from domestic biofuel burning for house heating, and therefore potentially transported mercury to the site. The slightly higher GOM could be caused by local photochemical transformation under low RH (54.7%).

The PBM concentrations were high in autumn, with a peak concentration of 57.63 pg m^{-3} . This is significantly higher than the concentrations in summer ($P < 0.05$) and in winter ($P < 0.001$) (Table S3). In the absence of volcanic sources, PBM concentrations are usually associated with Hg emission from anthropogenic activities (Friedli et al., 2003; Finley et al., 2009). There are several small villages in Shangri-La area. Due to high elevation (3850m above sea level), the weather was cold in autumn. For house heating, domestic biofuel burning from local anthropogenic sources could contribute to the high PBM level at SAWRS.

Back-trajectory analysis also suggested that high PBM events were associated with the air mass from Burma, Vietnam, Laos, Kampuchea and Thailand. Previous studies showed that the emission from the region could cause elevated TGM concentrations measured at a remote site (Sheu et al., 2013). Given the frequent air flows from the Southeast Asia to southwest China, similar transport events could also take place. The GOM and PBM levels were relatively lower from late spring to summer during the ISM period, likely due to the higher RF and RH (Table 1).

3.3 Air mass back trajectories analysis

Fig. 7 shows the time series of WD, RF and TGM with the calculated Indian Monsoon Index (IMI) during ISM months (April through September). The IMI values represent seasonal rainfall anomalies, and are highly correlated with the transport associated with ISM (Wang et al., 2001). An IMI value of >0 suggests

air transport from South Asia. Such a transport pattern was consistent from late May through mid-September. During the ISM period, WD was mainly from the southeast with relatively low wind speed (mean = 1.63 m s^{-1} in summer) and high precipitation. Although the mean TGM level in ISM period was relatively higher, the high TGM events did not persist throughout the entire ISM season. This suggested that the cumulus process and high RH could cause the low TGM level during ISM period.

There were three high TGM events shown in Fig.7 were further analyzed. Fig. 8 shows the back trajectories during April 26 to May 2 (first block in Fig.7). The air masses originated from Siberia moved over north Xinjiang, east Qinghai, Gansu and west Sichuan provinces. These are industrial areas in Northwest China that have major Hg emission sources (Fig. 1), mainly from the use of fossil fuels (Wang et al., 2000;Fu et al., 2008;Fu et al., 2012a;Fu et al., 2012c). From June 19 to July 2 (second block in Fig.7), the air mass was mainly from the Bengal and Burma because of the ISM (Fig. 9), suggesting trans-boundary transport possibly caused by anthropogenic sources in the region and the industrial cities (Fig. 1) such as Yangon (Burma's capital), Bangkok (Thailand's capital). Fig. 10 shows the back trajectories during September 17-22 (third block in Fig.7). Most trajectories in this period were very short and reached ground level (the endpoints were not shown after grounding). The elevated concentration in this event was likely to be contributed by the nearby domestic emissions.

3.4 Cluster analysis of back trajectories

The back trajectories arriving at the SAWRS over the study period were grouped into four clusters (Fig. 11) to show the synoptic air transport pattern and understand the regional transport pathways. Cluster analysis was performed to obtain the transport pattern. The cluster analysis showed the prevailing air masses arriving at Shangri-La and facilitated the identification of potential Hg source regions. Cluster 1 (19%) represented air masses originating from North Africa and had the highest trajectory elevation (Fig. 12). This indicated that the air masses passed quickly through Central Asia and then over Xinjiang, Qinghai provinces and Tibet of China. Cluster 2 (18%) and Cluster 3 (59%) were the air masses originating from South Asia and north India. The mean TGM concentration in Cluster 4 was significantly higher than the mean concentrations associated with the other three clusters (Table S4). Cluster 4, although relatively infrequent (4%), was associated with the highest TGM concentrations (mean = 3.9 ng m^{-3}) due to the passing of air masses over known source regions in Sichuan province. The area has a high background TGM level caused by industrial and domestic coal combustion, smelting industries, cement production, and biomass burning (Fu et al., 2008). Air masses of Cluster 3, the most frequent transport sector, also had high TGM concentrations (mean = 2.6 ng m^{-3}). Cluster 3 had the shortest trajectories that

1 move across Southeast Asian region where extensive biomass burning occurred during early spring. The
2 trajectory endpoints of Cluster 3 had relatively lower altitude (Fig. 12) and coincided with the fire
3 hotspots observed by MODIS satellite (Fig. S6), suggesting that the emissions from the biomass burning
4 can be transported to the SAWRS. TGM concentration (2.4 ng m^{-3}) associated with Cluster 2, also
5 frequent, could be linked to transport of atmospheric Hg from Pakistan and northern India including New
6 Delhi. Anthropogenic Hg emission in India has drawn increasing attention in recent years (Qureshi et al.,
7 2013). Air masses in Cluster 1 showed the lowest mean TGM concentration (2.3 ng m^{-3}) and originated
8 from Central Asia. This cluster was also associated with high wind speed caused by the strong prevailing
9 westerly in cold season.

11 The back trajectories of the upper quartile of TGM observations at the SAWRS are displayed in Fig. 13. It
12 is clear that the frequent transport from South and Southeast Asia during summer and autumn dominated
13 the high TGM observation at the SAWRS. The high concentrations associated with winter and spring
14 trajectories originated from Central Asia, North Africa and Mediterranean and then passed through
15 Middle East and Tibetan plateau were more likely caused by the domestic sources in China. The
16 relatively shorter trajectories from South Asia suggest that the transport from this sector may be caused by
17 slower air movement of the ISM (summer and early autumn). For lower quartile of TGM observations,
18 most back trajectories show the same directions as upper quartile of TGM observations (Fig.14). However,
19 back trajectories associated with the lower quartile of TGM observations were comparatively higher and
20 longer. These indicated that the air masses were traveling well above the planetary boundary layer where
21 ground based emission may not be incorporated in the air masses during low TGM period.

23 The potential sources and transport pathways of TGM at the SAWRS are shown in Fig. 15. It suggests
24 that Burma, Bengal bay, north India, west Sichuan Province and west Yunnan Province were the likely
25 source regions. Trans-boundary transport of aerosols released from forest fires and agricultural burning in
26 the Bengal bay region had been attributed to the seasonal changes of air movement caused by monsoons
27 (Reid et al., 2013). The PSCF analysis supports such trans-boundary transport events. Two high PSCF
28 values in India were also identified, including the surrounding areas of New Delhi and Uttar Pradesh.
29 Both are considered large urban regions with high industrial activities. Domestic source regions in
30 Sichuan and Yunnan were also identified. The atmospheric mercury concentrations observed at the
31 SAWRS were influenced by both domestic and foreign emission sources and highly dependent on the
32 seasonal winds that carry the air masses from different source regions to the observational site.

4 Conclusions

Measurements of TGM at a high-elevation background site in the southeastern corner of the Tibetan plateau from November 2009 to November 2010 show that the mean TGM (2.55 ng m^{-3}) was higher than typical background levels observed in the Northern Hemisphere ($1.5\text{--}1.7 \text{ ng m}^{-3}$). Significant seasonal variability in TGM concentration due to meteorological factors and long-range transport influenced by the ISM and Westerlies was also observed. The ISM increased the TGM levels occasionally by carrying TGM-enriched air from South Asia, while moist air from the ISM decreased GOM and PBM levels. The Westerlies could also carry the Hg emissions from the domestic sources in China to the site when the air masses moved over those source regions. The TGM concentration was higher during the daytime mainly due to upslope transport of polluted air from lower-altitude areas around the site. High GOM levels were highly correlated with dry air in autumn and winter, and in-situ photochemical production might have contributed to occasionally high GOM concentration. Cluster analysis of backward trajectories suggested that Southeast Asia and Mainland China are the most important source regions to this site.

Acknowledgements. This work is supported by National “973” Program (2013CB430003), and Natural Science Foundation of China (41273145, 41003051). We also thank the staff of Meteorological Bureau of Diqing Tibetan Autonomous Prefecture for field sampling assistance.

References

- AMAP/UNEP: Technical Background Report for the Global Mercury Assessment 2013, in, Arctic Monitoring and Assessment Programme, Oslo, Norway/UNEP Chemicals Branch Geneva, Switzerland, 2013.
- Carpi, A., and Lindberg, S. E.: Application of a Teflon (TM) dynamic flux chamber for quantifying soil mercury flux: Tests and results over background soil, *Atmospheric Environment*, 32, 873-882, 1998.
- Dorling, S. R., Davies, T. D., and Pierce, C. E.: Cluster-Analysis - a Technique for Estimating the Synoptic Meteorological Controls on Air and Precipitation Chemistry - Results from Eskdalemuir, South Scotland, *Atmospheric Environment Part a-General Topics*, 26, 2583-2602, 1992.
- Driscoll, C. T., Mason, R. P., Chan, H. M., Jacob, D. J., and Pirrone, N.: Mercury as a Global Pollutant: Sources, Pathways, and Effects, *Environmental science & technology*, 47, 4967-4983, doi:10.1021/es305071v, 2013.
- Fain, X., Obrist, D., Hallar, A., Mccubbin, I., and Rahn, T.: High levels of reactive gaseous mercury observed at a high elevation research laboratory in the Rocky Mountains, *Atmospheric Chemistry and Physics*, 9, 8049-8060, doi:10.5194/acp-9-8049-2009, 2009.
- Feng, X., Sommar, J., Gårdfeldt, K., and Lindqvist, O.: Improved determination of gaseous divalent mercury in ambient air using KCl coated denuders, *Fresenius' journal of analytical chemistry*, 366, 423-428, 2000.
- Finley, B., Swartzendruber, P., and Jaffe, D.: Particulate mercury emissions in regional wildfire plumes observed at the Mount Bachelor Observatory, *Atmospheric Environment*, 43, 6074-6083, 2009.
- Friedli, H., Radke, L., Prescott, R., Hobbs, P., and Sinha, P.: Mercury emissions from the August 2001 wildfires in Washington State and an agricultural waste fire in Oregon and atmospheric mercury budget estimates, *Cy.*, 17, 1039, doi:10.1029/2002GB001972, 2003.

1 Fu, X., Feng, X., Zhu, W., Wang, S., and Lu, J.: Total gaseous mercury concentrations in ambient air in
 2 the eastern slope of Mt. Gongga, South-Eastern fringe of the Tibetan plateau, China, *Atmospheric*
 3 *Environment*, 42, 970-979, 2008.
 4 Fu, X., Feng, X., Dong, Z., Yin, R., Wang, J., Yang, Z., and Zhang, H.: Atmospheric gaseous elemental
 5 mercury(GEM) concentrations and mercury depositions at a high-altitude mountain peak in south China,
 6 *Atmospheric Chemistry and Physics*, 10, 2425-2437, doi:10.5194/acp-10-2425-2010, 2010.
 7 Fu, X., Feng, X., Qiu, G., Shang, L., and Zhang, H.: Speciated atmospheric mercury and its potential
 8 source in Guiyang, China, *Atmospheric Environment*, 45, 4205-4212, 2011.
 9 Fu, X., Feng, X., Liang, P., Zhang, H., Ji, J., and Liu, P.: Temporal trend and sources of speciated
 10 atmospheric mercury at Waliguan GAW station, Northwestern China, *Atmospheric Chemistry and Physics*,
 11 12, 1951-1964, doi:10.5194/acp-12-1951-2012, 2012a.
 12 Fu, X., Feng, X., Shang, L., Wang, S., and Zhang, H.: Two years of measurements of atmospheric total
 13 gaseous mercury (TGM) at a remote site in Mt. Changbai area, Northeastern China, *Atmospheric*
 14 *Chemistry and Physics*, 12, 4215-4226, doi:10.5194/acp-12-4215-2012, 2012b.
 15 Fu, X., Feng, X., Sommar, J., and Wang, S.: A review of studies on atmospheric mercury in China,
 16 *Science of the Total Environment*, 421, 73-81, 2012c.
 17 Gay, D. A., Schmeltz, D., Prestbo, E., Olson, M., Sharac, T., and Tordon, R.: The Atmospheric Mercury
 18 Network: measurement and initial examination of an ongoing atmospheric mercury record across North
 19 America, *Atmospheric Chemistry and Physics*, 13, 11339-11349, 2013.
 20 Goodsite, M. E., Plane, J., and Skov, H.: A theoretical study of the oxidation of Hg⁰ to HgBr₂ in the
 21 troposphere, *Environmental science & technology*, 38, 1772-1776, 2004.
 22 Graydon, J. A., St. Louis, V. L., Lindberg, S. E., Hintelmann, H., and Krabbenhoft, D. P.: Investigation of
 23 mercury exchange between forest canopy vegetation and the atmosphere using a new dynamic chamber,
 24 *Environmental science & technology*, 40, 4680-4688, 2006.
 25 Guey-Rong Sheu, Neng-Huei Lin, Chung-Te Lee, Jia-Lin Wang, Ming-Tung Chuang, Sheng-Hsiang
 26 Wang, Kai Hsine Chi, Chang-Feng Ou-Yang: Distribution of atmospheric mercury in northern Southeast
 27 Asia and South China Sea during Dongsha Experiment, *Atmospheric Environment*, 78, 174-183, 2013
 28 Iverfeldt, Å., and Lindqvist, O.: Atmospheric oxidation of elemental mercury by ozone in the aqueous
 29 phase, *Atmospheric Environment* (1967), 20, 1567-1573, 1986.
 30 J. Munthe, I. W. angberg, N. Pirrone, A. Iverfeldt, R. Ferrara, R. Ebinghaus, X. Feng, K. Gardfeldt, G.
 31 Keeler, E. Lanzillotta, S.E. Lindberg, J. Luh, Y. Mamane, E. Prestbo, S. Schmolke, W.H. Schroeder,
 32 J. Sommar, F. Sprovieri, R.K. Stevens, W. Stratton, G. Tuncel, A. Urba, Intercomparison of methods for
 33 sampling and analysis of atmospheric mercury species, *Atmospheric Environment*, 35, 3007-3017, 2001.
 34 Jaffe, D., Prestbo, E., Swartzendruber, P., Weiss-Penzias, P., Kato, S., Takami, A., Hatakeyama, S., and
 35 Kajii, Y.: Export of atmospheric mercury from Asia, *Atmospheric Environment*, 39, 3029-3038, 2005.
 36 Johansson, K., Bergbäck, B., and Tyler, G.: Impact of atmospheric long range transport of lead, mercury
 37 and cadmium on the Swedish forest environment, *Water, Air, & Soil Pollution: Focus*, 1, 279-297, 2001.
 38 Kock, H., Bieber, E., Ebinghaus, R., Spain, T., and Thees, B.: Comparison of long-term trends and
 39 seasonal variations of atmospheric mercury concentrations at the two European coastal monitoring
 40 stations Mace Head, Ireland, and Zingst, Germany, *Atmospheric Environment*, 39, 7549-7556, 2005.
 41 Landis, M. S., Stevens, R. K., Schaedlich, F., and Prestbo, E. M.: Development and characterization of an
 42 annular denuder methodology for the measurement of divalent inorganic reactive gaseous mercury in
 43 ambient air, *Environmental Science & Technology*, 36, 3000-3009, 2002a.
 44 Landis, M. S., Vette, A. F., and Keeler, G. J.: Atmospheric mercury in the Lake Michigan basin: Influence
 45 of the Chicago/Gary urban area, *Environmental Science & Technology*, 36, 4508-4517, 2002b.
 46 Li, J., and Lee, S. M.: Progress of Global Atmospheric Mercury Field Observations, *Journal of Clean*
 47 *Energy Technologies*, 2, 252-257, doi:10.7763/JOCET.2014.V2.135, 2014..
 48 Lin, C. J., and Pehkonen, S. O.: The chemistry of atmospheric mercury: a review, *Atmospheric*
 49 *Environment*, 33, 2067-2079, 1999.
 50 Lindberg, S.: Forests and the global biogeochemical cycle of mercury: the importance of understanding
 51 air/vegetation exchange processes, in: *Global and Regional Mercury Cycles: Sources, Fluxes and Mass*

1 Balances, Springer, 359-380, 1996.

2 Lindberg, S., Bullock, R., Ebinghaus, R., Engstrom, D., Feng, X., Fitzgerald, W., Pirrone, N., Prestbo, E.,
3 and Seigneur, C.: A synthesis of progress and uncertainties in attributing the sources of mercury in
4 deposition, *AMBIO: A Journal of the Human Environment*, 36, 19-33, 2007.

5 Lindberg, S. E., Brooks, S., Lin, C.-J., Scott, K. J., Landis, M. S., Stevens, R. K., Goodsite, M., and
6 Richter, A.: Dynamic oxidation of gaseous mercury in the Arctic troposphere at polar sunrise,
7 *Environmental science & technology*, 36, 1245-1256, 2002.

8 Lindqvist, O.: Mercury in the Swedish environment: recent research on causes, consequences and
9 corrective methods, *Water, air and soil pollution*, 55, 1-261, 1991.

10 Loewen, M., Kang, S., Armstrong, D., Zhang, Q., Tomy, G., and Wang, F.: Atmospheric transport of
11 mercury to the Tibetan Plateau, *Environmental Science & Technology*, 41, 7632-7638, 2007.

12 Mary M. Lynam, Gerald J. Keeler, Comparison of methods for particulate phase mercury
13 analysis:sampling and analysis, *Anal Bioanal Chem*, 374, 1009–1014, DOI: 10.1007/s00216-002-1584-4,
14 2002.

15 Nguyen, H. T., Kim, K. H., Kim, M. Y., Hong, S., Youn, Y. H., Shon, Z. H., and Lee, J. S.: Monitoring of
16 atmospheric mercury at a global atmospheric watch (GAW) site on An-Myun Island, Korea, *Water, Air, &
17 Soil Pollution*, 185, 149-164, 2007.

18 Obrist, D., Hallar, A., McCubbin, I., Stephens, B. B., and Rahn, T.: Atmospheric mercury concentrations
19 at Storm Peak Laboratory in the Rocky Mountains: Evidence for long-range transport from Asia,
20 boundary layer contributions, and plant mercury uptake, *Atmospheric Environment*, 42, 7579-7589, 2008.

21 Pacyna, E. G., Pacyna, J. M., Steenhuisen, F., and Wilson, S.: Global anthropogenic mercury emission
22 inventory for 2000, *Atmospheric Environment*, 40, 4048-4063, 2006.

23 Poissant, L., and Casimir, A.: Water-air and soil-air exchange rate of total gaseous mercury measured at
24 background sites, *Atmospheric Environment*, 32, 883-893, 1998.

25 Pfaffhuber, K., Berg, T., Hirdman, D., and Stohl, A.: Atmospheric mercury observations from Antarctica:
26 seasonal variation and source and sink region calculations, *Atmospheric Chemistry and Physics*, 12,
27 3241-3251, 2012.

28 Pirrone, N., Keeler, G. J., and Nriagu, J. O.: Regional differences in worldwide emissions of mercury to
29 the atmosphere, *Atmospheric Environment*, 30, 2981-2987, 1996.

30 Pirrone, N., Costa, P., Pacyna, J., and Ferrara, R.: Mercury emissions to the atmosphere from natural and
31 anthropogenic sources in the Mediterranean region, *Atmospheric Environment*, 35, 2997-3006, 2001.

32 Pirrone, N., Cinnirella, S., Feng, X., Finkelman, R., Friedli, H., Leaner, J., Mason, R., Mukherjee, A.,
33 Stracher, G., and Streets, D.: Global mercury emissions to the atmosphere from anthropogenic and natural
34 sources, *Atmospheric Chemistry and Physics*, 10, 5951-5964, doi:10.5194/acp-10-5951-2010, 2010.

35 Polissar, A. V., Hopke, P. K., and Harris, J. M.: Source regions for atmospheric aerosol measured at
36 Barrow, Alaska, *Environmental science & technology*, 35, 4214-4226, 2001.

37 Qureshi, A., Vadenbo, C., and Hellweg, S.: Anthropogenic mercury flows in India and impacts of
38 emission controls, *Environmental science & technology*, 47, 8105–8113, doi:10.1021/es401006k, 2013..

39 Reid, J. S., Hyer, E. J., Johnson, R. S., Holben, B. N., Yokelson, R. J., Zhang, J., Campbell, J. R.,
40 Christopher, S. A., Di Girolamo, L., and Giglio, L.: Observing and understanding the Southeast Asian
41 aerosol system by remote sensing: An initial review and analysis for the Seven Southeast Asian Studies
42 (7SEAS) program, *Atmospheric Research*, 122, 403-468, 2013.

43 Rozwadowska, A., Zielinski, T., Petelski, T., and Sobolewski, P.: Cluster analysis of the impact of air
44 back-trajectories on aerosol optical properties at Hornsund, Spitsbergen, *Atmospheric Chemistry and
45 Physics*, 10, 877-893, 2010.

46 Seo, Y.-S., Han, Y.-J., Choi, H.-D., Holsen, T. M., and Yi, S.-M.: Characteristics of total mercury (TM)
47 wet deposition: scavenging of atmospheric mercury species, *Atmospheric Environment*, 49, 69-76, 2012.

48 Schroeder, W. H., and Munthe, J.: Atmospheric mercury--an overview, *Atmospheric Environment*, 32,
49 809-822, 1998.

50 Schwesig, D., and Krebs, O.: The role of ground vegetation in the uptake of mercury and methylmercury
51 in a forest ecosystem, *Plant and Soil*, 253, 445-455, 2003.

Sharma, D. C.: Concern over mercury pollution in India, *The Lancet*, 362, 1050, 2003.

Sheu, G.-R., Lin, N.-H., Lee, C.-T., Wang, J.-L., Chuang, M.-T., Wang, S.-H., Chi, K. H., and Ou-Yang, C.-F.: Distribution of atmospheric mercury in northern Southeast Asia and South China Sea during Dongsha Experiment, *Atmospheric Environment*, 78, 174-183, 2013.

Sprovieri, F., Gratz, L., and Pirrone, N.: Development of a Ground-Based Atmospheric Monitoring Network for the Global Mercury Observation System (GMOS), *E3S Web of Conferences*, 17007, Rome, Italy, 22–27 September 2012, doi:10.1051/e3sconf/20130117007, 2013.

Steffen, A., Bottenheim, J., Cole, A., Ebinghaus, R., Lawson, G., and Leaitch, W.: Atmospheric mercury speciation and mercury in snow over time at Alert, Canada, *Atmospheric Chemistry and Physics*, 14, 2219-2231, doi: 10.5194/acp-14-2219-2014, 2014.

Streets, D. G., Hao, J., Wu, Y., Jiang, J., Chan, M., Tian, H., and Feng, X.: Anthropogenic mercury emissions in China, *Atmospheric Environment*, 39, 7789-7806, 2005.

Sunderland, E. M., Krabbenhoft, D. P., Moreau, J. W., Strode, S. A., and Landing, W. M.: Mercury sources, distribution, and bioavailability in the North Pacific Ocean: Insights from data and models, *Cy.*, 23, GB2010, doi:10.1029/2008GB003425, 2009.

Valente, R. J., Shea, C., Lynn Humes, K., and Tanner, R. L.: Atmospheric mercury in the Great Smoky Mountains compared to regional and global levels, *Atmospheric Environment*, 41, 1861-1873, 2007.

Wang, B., and Fan, Z.: Choice of South Asian summer monsoon indices, *Bulletin of the American Meteorological Society*, 80, 629-638, 1999.

Wang, B., Wu, R., and Lau, K.: Interannual Variability of the Asian Summer Monsoon: Contrasts between the Indian and the Western North Pacific-East Asian Monsoons*, *Journal of Climate*, 14, 4073-4090, 2001.

Wang, Q., Shen, W., and Ma, Z.: Estimation of mercury emission from coal combustion in China, *Environmental science & technology*, 34, 2711-2713, 2000.

Wang, Y. Q., Zhang, X. Y., and Draxler, R. R.: TrajStat: GIS-based software that uses various trajectory statistical analysis methods to identify potential sources from long-term air pollution measurement data, *Environmental Modelling & Software*, 24, 938-939, 2009.

Xiao, Z., Sommar, J., Wei, S., and Lindqvist, O.: Sampling and determination of gas phase divalent mercury in the air using a KCl coated denuder, *Fresenius' journal of analytical chemistry*, 358, 386-391, 1997.

Xu, B., Cao, J., Hansen, J., Yao, T., Joswita, D. R., Wang, N., Wu, G., Wang, M., Zhao, H., and Yang, W.: Black soot and the survival of Tibetan glaciers, *Proceedings of the National Academy of Sciences*, 106, 22114-22118, 2009.

Yang, Y., Chen, H., and Wang, D.: Spatial and temporal distribution of gaseous elemental mercury in Chongqing, China, *Environmental monitoring and assessment*, 156, 479-489, 2009.

Zhang, Q., Huang, J., Wang, F., Mark, L., Xu, J., Armstrong, D., Li, C., Zhang, Y., and Kang, S.: Mercury Distribution and Deposition in Glacier Snow over Western China, *Environmental Science & Technology*, 46, 5404-5413, 2012.

1 **Table 1:**The seasonal statistics of the measured TGM、GOM、PBM、WS、AT、RH and RF from November
2 2009 through November 2010 at the SAWRS site. N is the number of samples.

		TGM (ng m ⁻³)	GOM (pg m ⁻³)	PBM (pg m ⁻³)	AT (°C)	RH (%)	WS (m s ⁻¹)	RF (mm)
Spring Mar–May	Mean	2.76	3.20	33.53	4.85	78.06	1.98	34.07
	St. Dev.	0.87	3.27	25.05	3.32	12.88	0.63	
	Median	2.6	2.12	27.28	4.05	79.5	1.9	
	Range	1.43-13.59	0.71-16.69	3.80-112.82	-0.4-13	37-98	0.7-3.4	
	N	18706	43	46	2160	2160	2160	90
Summer Jun–Aug	Mean	2.51	3.96	26.14	12.37	85.97	1.63	183.97
	St. Dev.	0.71	3.82	18.17	1.59	7.91	0.61	
	Median	2.35	2.85	22.33	12.4	87	1.5	
	Range	1.05-6.11	0.77-18.81	3.02-86.97	7.2-15.6	65-99	0.5-3.4	
	N	17662	80	69	2280	2280	2280	95
Autumn Sep–Nov	Mean	2.71	7.60	57.63	6.25	84.46	1.5	38.17
	St. Dev.	0.79	6.15	36.49	3.61	8.39	0.44	
	Median	2.59	5.27	45.82	6.3	84.5	1.5	
	Range	1.03-6.99	0.78-31.09	10.93-185.06	-0.3-11.7	63-99	0.4-2.66	
	N	13161	103	100	2280	2280	2280	95
Winter Dec–Feb	Mean	2.28	14.62	21.36	-1.37	54.68	2.34	0
	St. Dev.	0.42	9.12	15.72	1.64	16.98	0.72	
	Median	2.22	13.09	15.23	-1.11	58	2.25	
	Range	1.18-4.51	2.70-39.85	3.76-65.9	-6.6-1.6	19-84	0.9-4.3	
	N	20003	97	53	2256	2256	2256	94
Total	Mean	2.55	8.22	38.32	5.57	75.97	1.86	
	St. Dev.	0.73	7.90	31.26	5.57	16.81	0.68	
	Median	2.39	5.16	30.67	5.1	79	1.8	
	Range	1.03-13.59	0.71-39.85	3.02-185.59	-6.6-15.6	19-99	0.4-4.3	
	N	69532	323	268	8976	8976	8976	374

3

Fig. 1: Map showing the location of SAWRS, anthropogenic Hg emissions ($\text{g km}^{-2} \text{y}^{-1}$) and major cities in Asia (AMAP/UNEP, 2013).

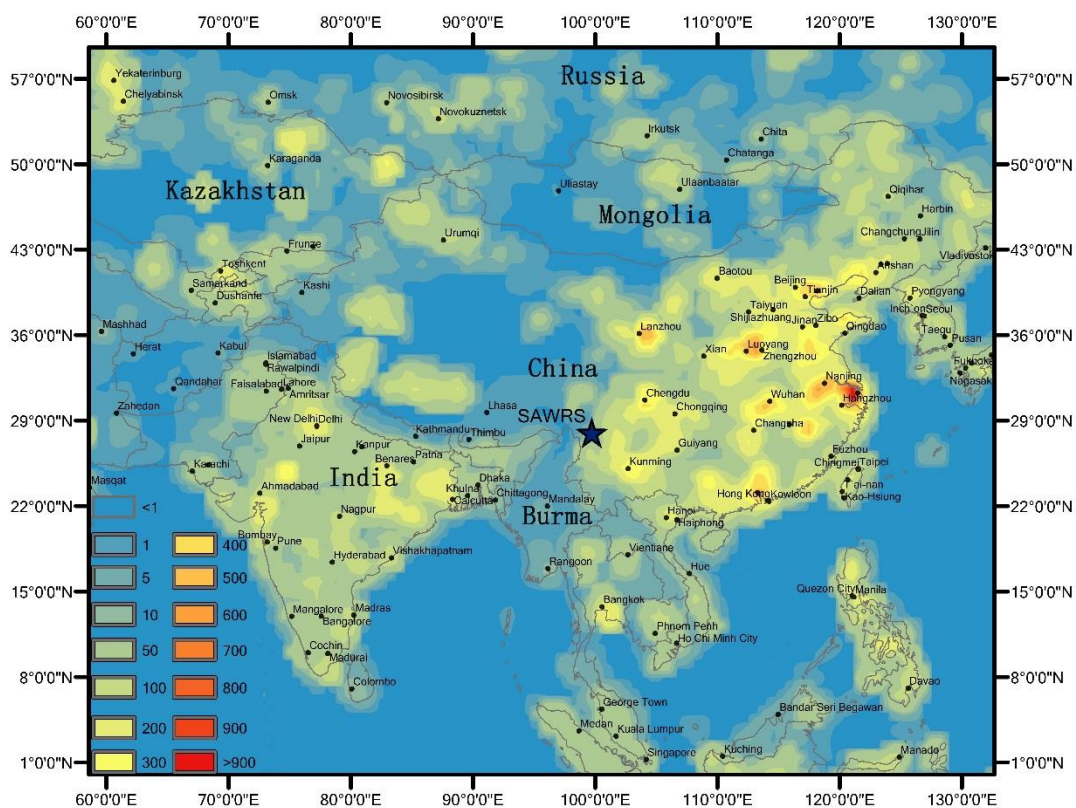
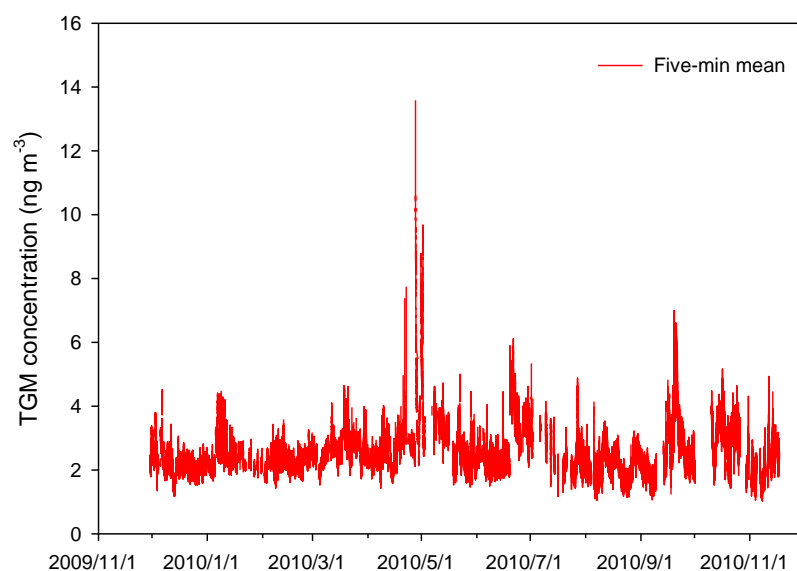
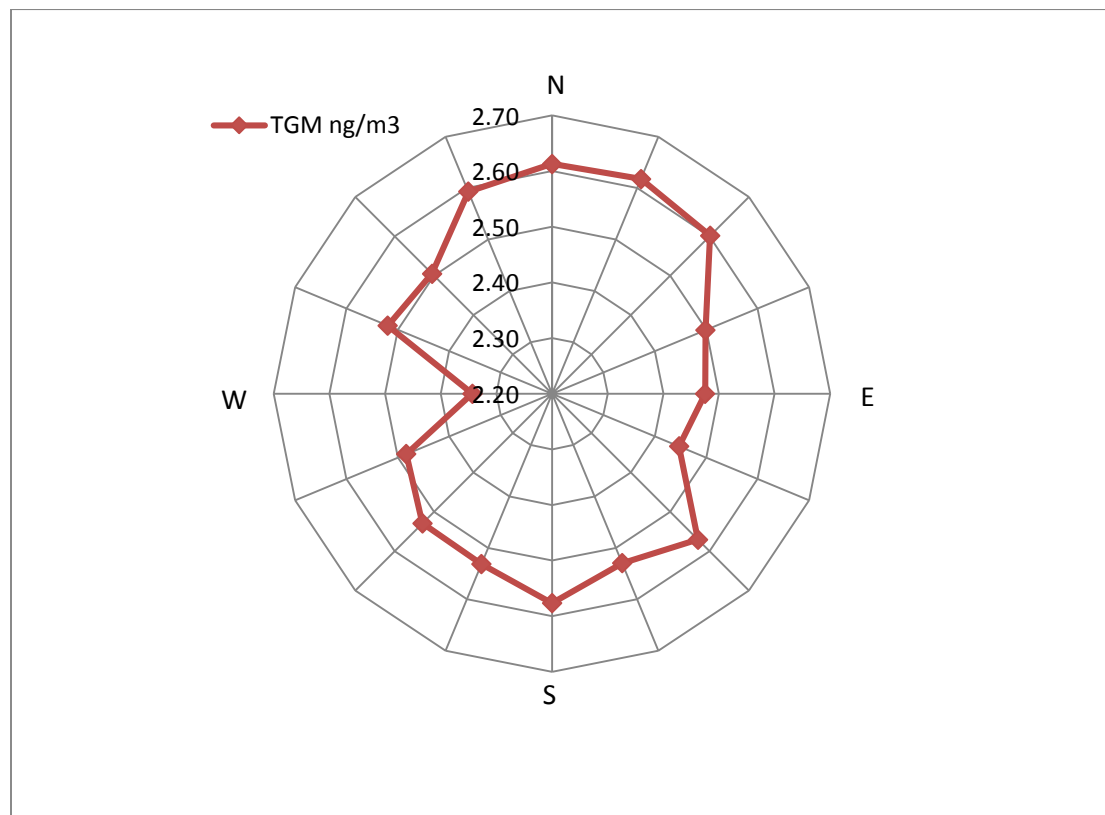


Fig. 2: The 5-min time series distribution of TGM concentrations at SAWRS in the campaign, spikes of high TGM concentrations were observed from late April through early May, from late June through early July and in late September, respectively.

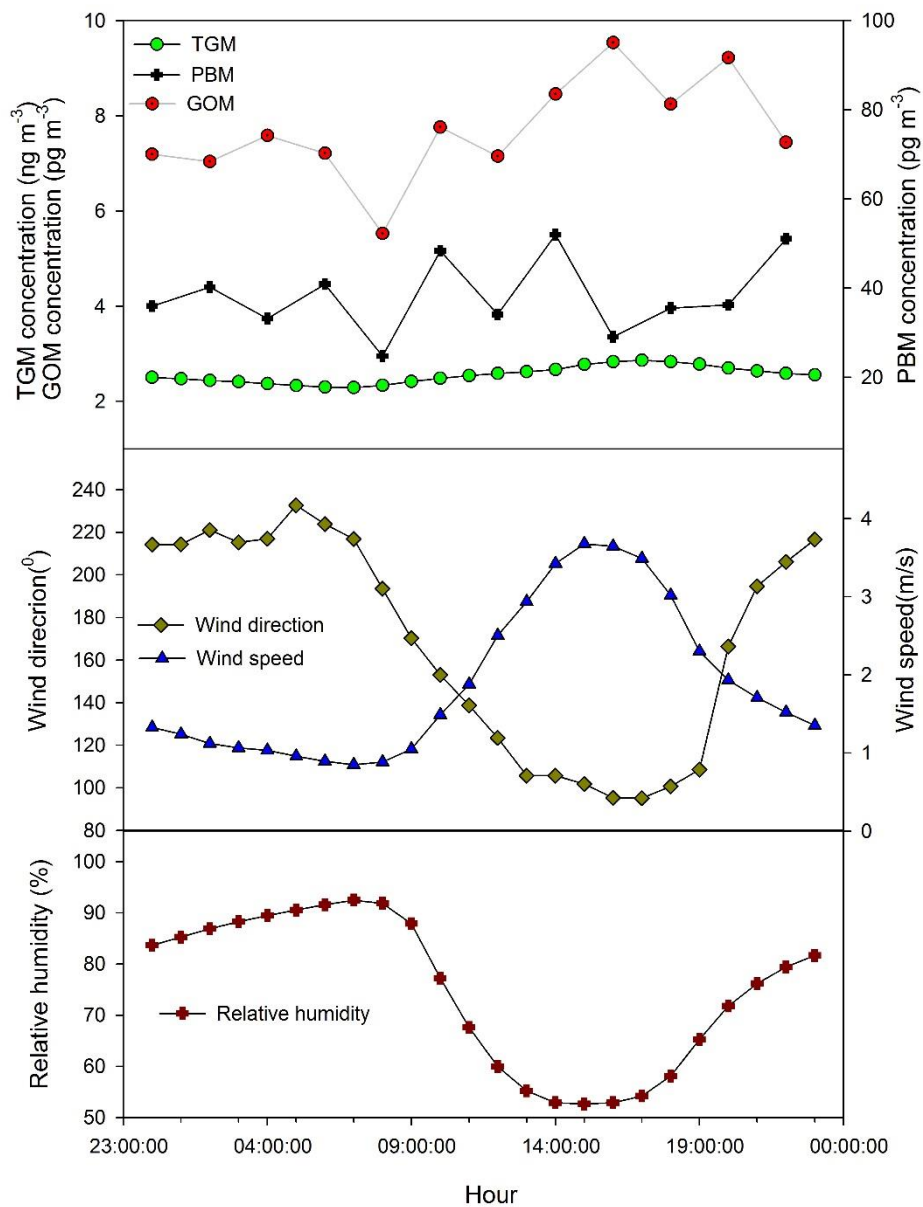


1 **Fig. 3:** The concentration wind rose at SAWRS, TGM concentration exhibited a strong dependence on
 2 wind direction. Higher TGM levels were frequently associated with northerly winds.



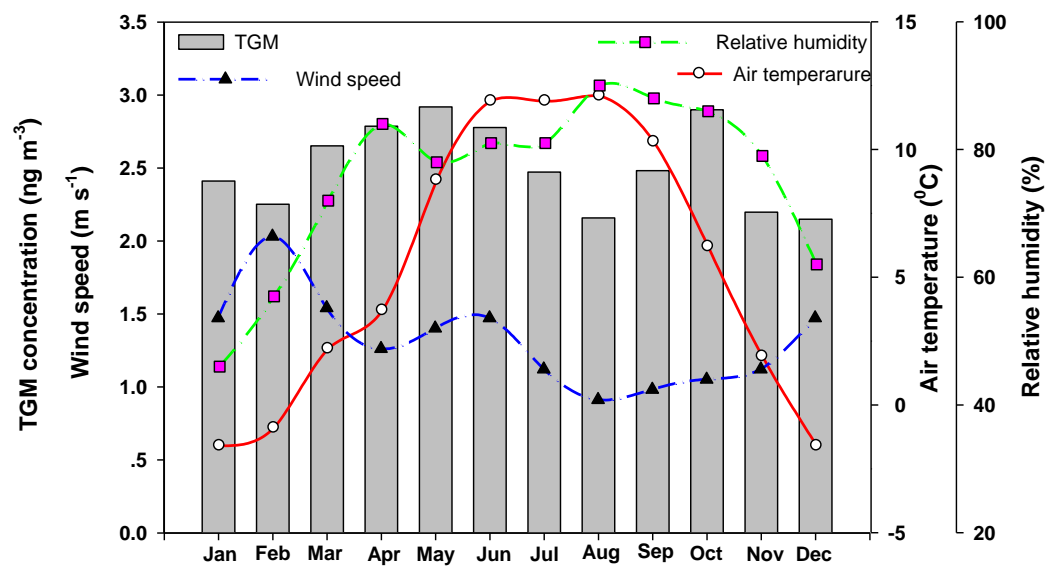
3
4
5

1 **Fig. 4:** The diurnal variation of TGM, GOM and PBM with WD,WS and RH.



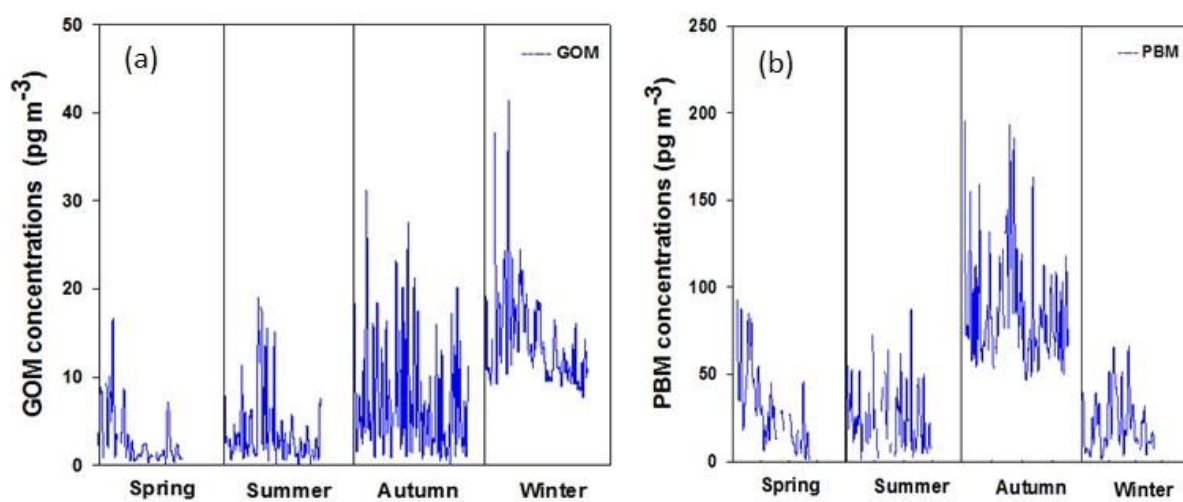
2

1 **Fig. 5:** The variation of the monthly means of TGM, WS, AT and RH. High TGM concentration in ISM
2 period with high AT and RH.



3
4

1 **Fig. 6:** Seasonal variability of GOM and PBM during four sampling campaigns.



2

3

Fig. 7: Time series of WD, RF and TGM and the calculated Indian Monsoon Index (IMI) from April to September 2010. An IMI value >0 indicates air movement from south toward north, which is also associated with greater precipitation. WD measured at the SAWRS was mostly from the southeast. Zero IMI indicates weak air movement. Negative IMI indicates northerly wind that push the air back the Indian Ocean. Highlighted in red represent the causes of these events are not only impacted by local airflow but also long-term transportation; while blue just represent the local airflow impact.

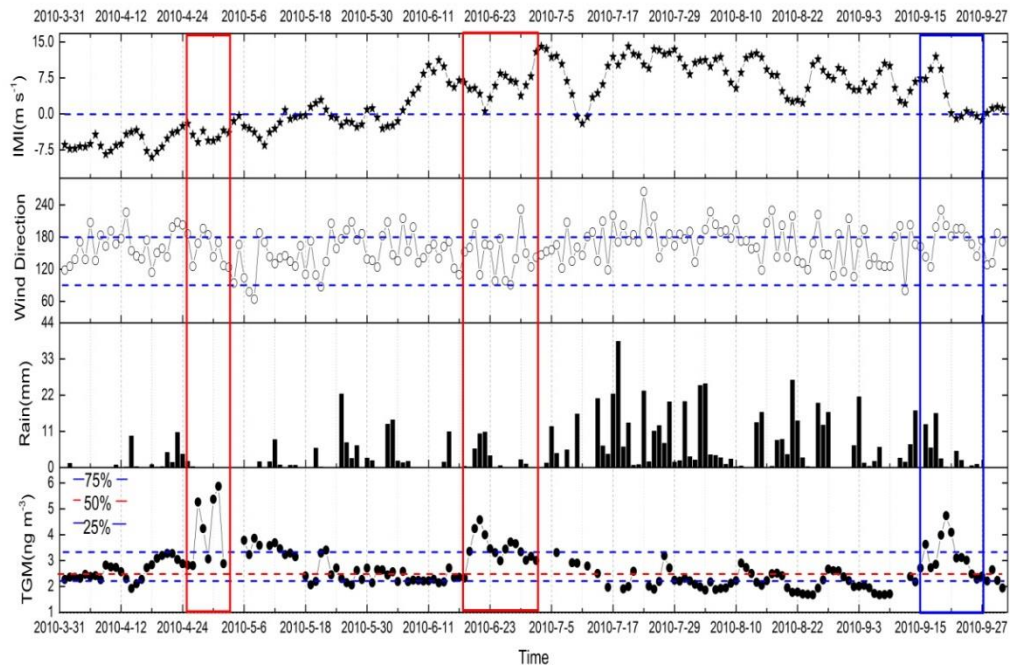
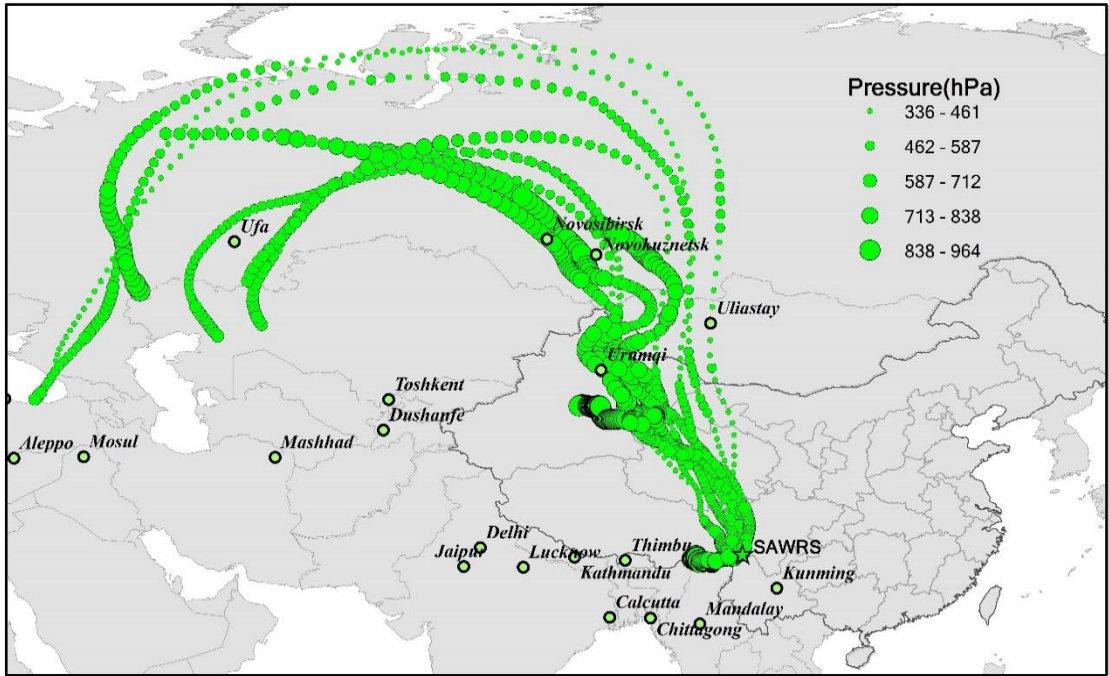
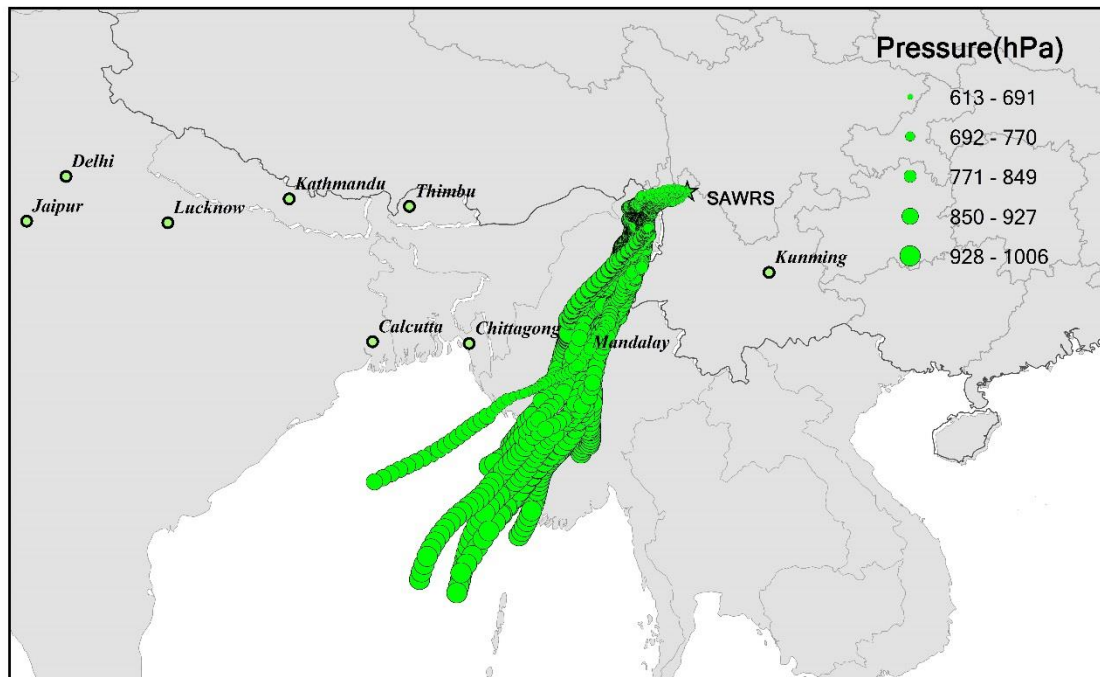


Fig. 8: The back trajectories of air masses from April 26 to May 2. The high pressure means that the height of trajectories are low, therefore the air masses can easily transport mercury emitted from surface to SAWRS.

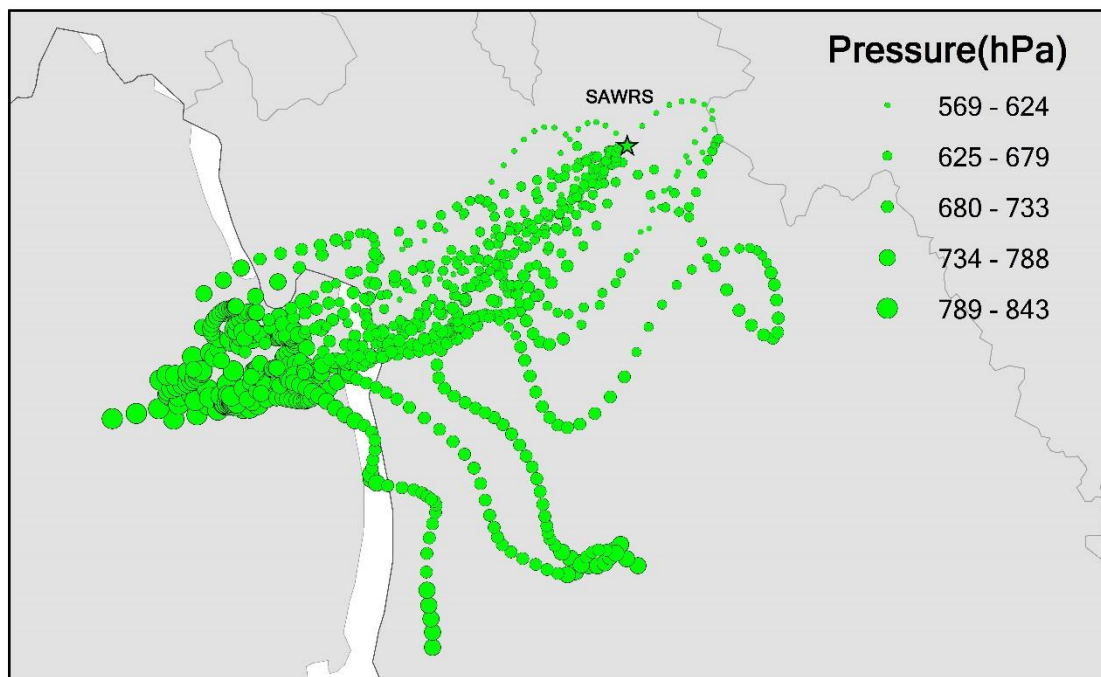


1 **Fig. 9:** The back trajectories of air mass from June19 to July 2.



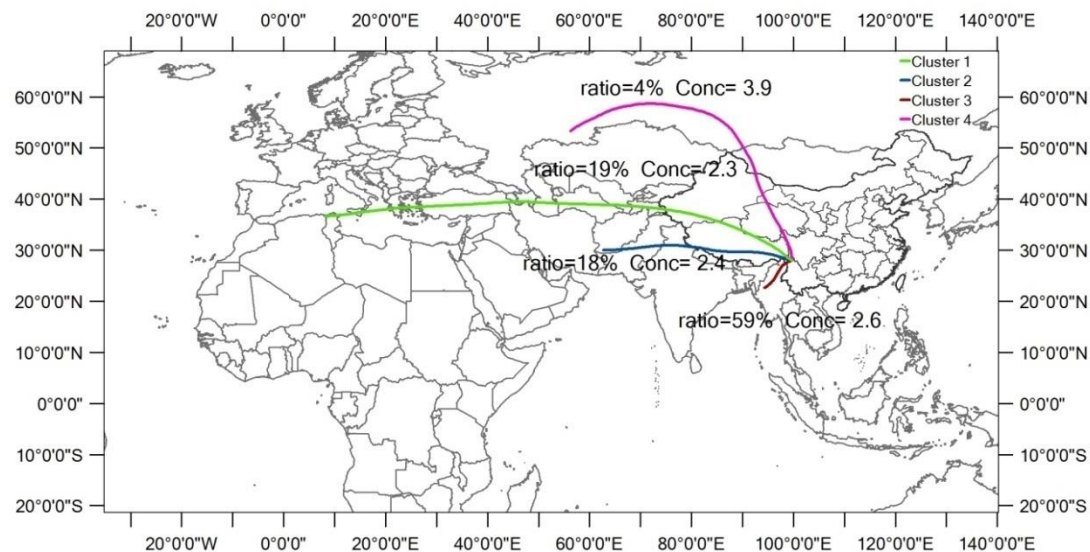
2
3

1 **Fig. 10:** The back trajectories of air mass from September 17 to 22. The trajectory points reaching the
2 ground level are not shown in the figure.

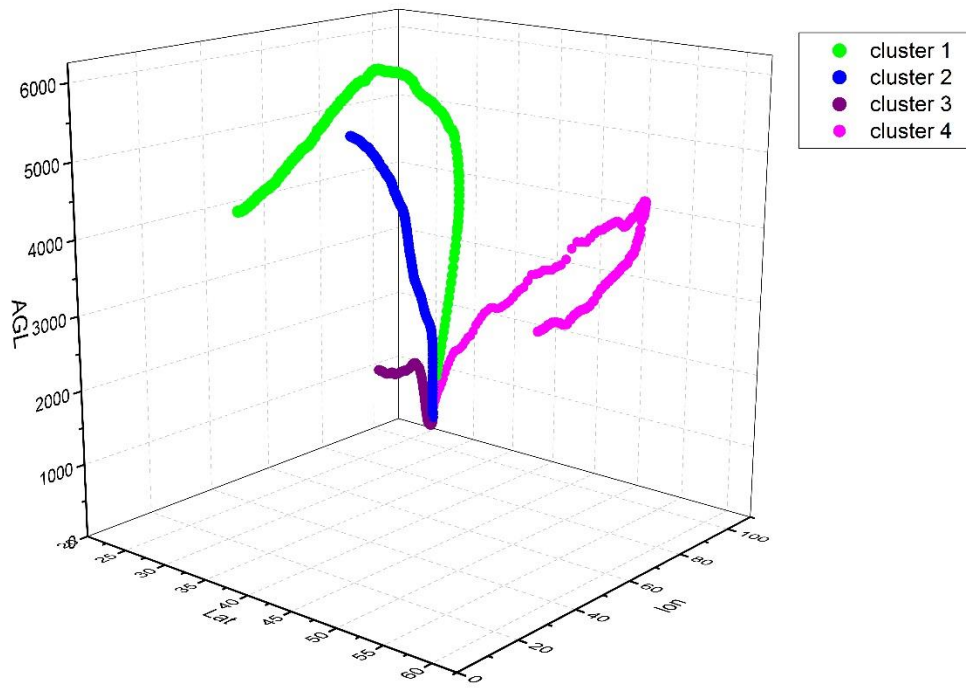


3
4

Fig. 11: The back trajectories arriving at the SAWRS over the study period were grouped into four clusters. Most of air masses originated from Southeast Asia (Cluster 3, 59%), considerable air masses originated from North Africa and south Asia (Cluster 1, 19%; Cluster 2, 18%), only 4% of air masses originated from Central Asia and Russia.



1 **Fig. 12:** The three-dimensional height of all the clusters from different direction at SAWRS.



2
3
4
5

Fig. 13: The back trajectories of the upper quartile of TGM observations at the SAWRS in the four seasons. The air masses with high Hg from South and Southeast Asia in summer and autumn, while some air masses with high Hg were from northwest China. The rest of the air masses were from west Asia, Central Asia and Tibetan plateau in spring and winter.

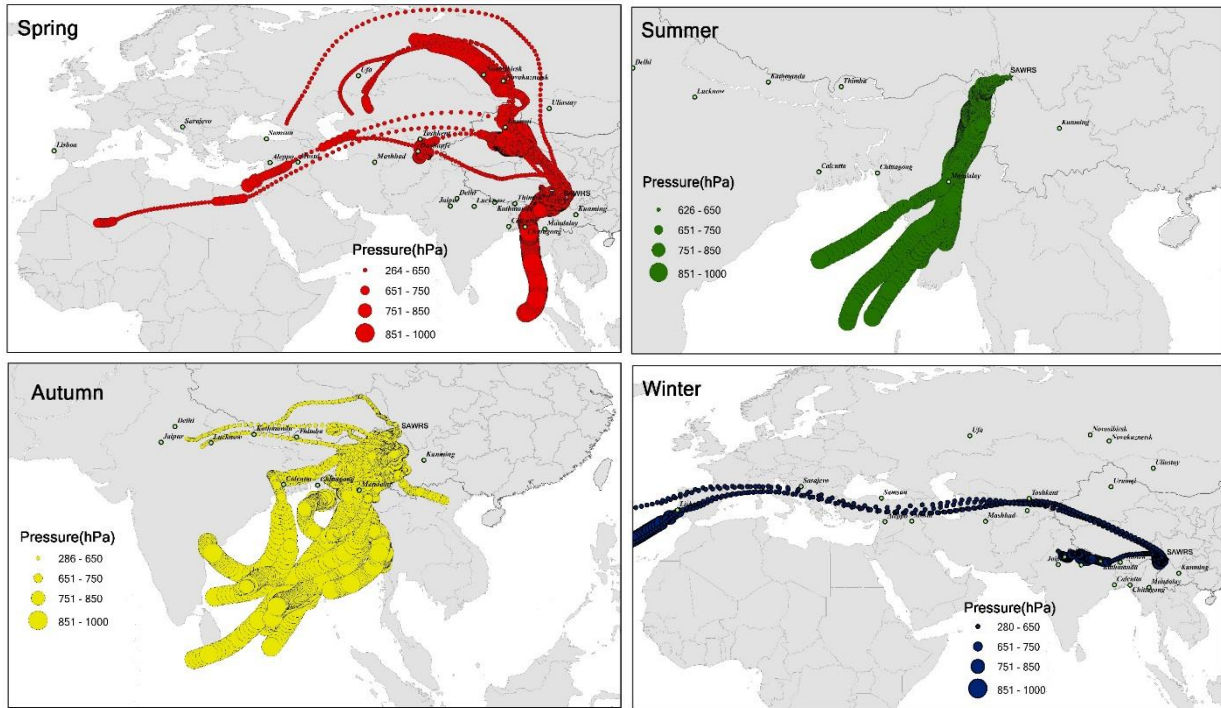


Fig. 14: The back trajectories associated with the lower quartile of TGM observations in the four seasons. The air masses with low Hg from South and Southeast Asia in autumn and summer. The rest of the air masses were from west Asia, Central Asia and Tibetan plateau.

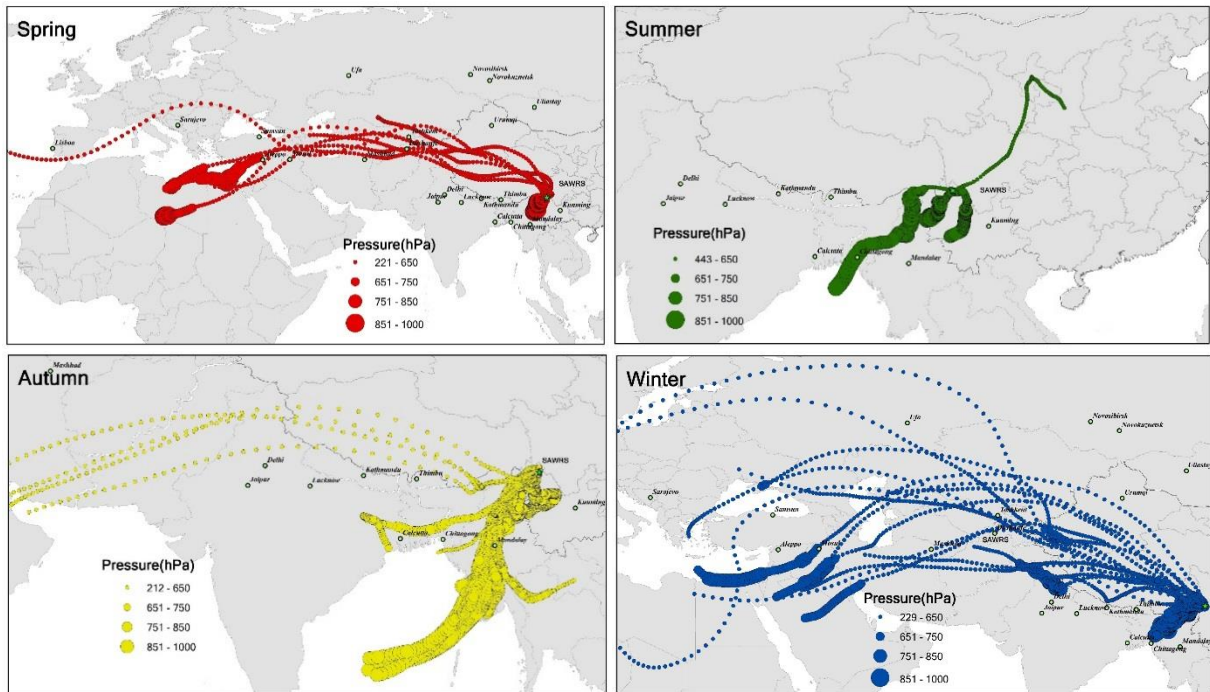


Fig. 15: The potential sources and transport pathways of TGM at the SAWRS identified by the PSCF. Burma, Bengal bay, north India, western Sichuan Province and western Yunnan Province were likely the potential source regions for Shangri-La.

